Available online at www.sciencedirect.com
SCIENCE DIRECT
Biomass and Bioenergy 30 (2006) 684–691
BIOMASS & BIOENERGY
www.elsevier.com/locate/biombioe

Part II: Computational studies on a pulverised fuel stove

C.S. Bhaskar Dixit[a,*], P.J. Paul[b], H.S. Mukunda[b]

[a]Department of Mechanical Engineering, Bapuji Institute of Engineering and Technology, Davanagere 577 004, India
[b]Combustion Gasification and Propulsion Laboratory, Indian Institute of Science, Bangalore 560 012, India

Received 23 November 2004; received in revised form 9 December 2005; accepted 20 January 2006
Available online 11 April 2006

Abstract

This paper presents computational and analytical studies made on the pulverised fuel stove reported in part I (Dixit CSB, Paul PJ, Mukunda HS. Experimental studies on a pulverised fuel stove. Biomass and Bioenergy, to be published).

An analysis has been carried out on the condensed phase thermal profile with moving pyrolysis front for this stove. This unsteady thermal analysis that accounts for moving pyrolysis front has provided the predictions for the rate of movement of the pyrolysis front. The comparison of the predicted temperature profiles and pyrolysis front movement rates with the measured data is excellent.

The single port configuration was computationally analysed with an aim to understand the aero-thermo-chemical behaviour of the stove operation in combustion and gasification modes. The g-phase of tangential entry stove was subjected to a three-dimensional analysis using a commercial CFD code CFX TASCflow with combustion modelled using single step overall reaction. It was possible to obtain combustion and gasification modes of stove operation computationally also by varying the fuel release pattern. A fuel release pattern biased towards the bottom of the port as seen in the experiments, when used for the calculations, resulted in gasification mode operation while uniform fuel release pattern induced combustion mode operation. Comparison of g-phase temperature profiles in combustion mode seems satisfactory. The comparison of g-phase temperature profiles in the gasification mode appears intriguing. An explanation for the behaviour is sought in faster hydrogen combustion compared to carbon monoxide, something not accounted for in the calculations with single step chemistry.

Keywords: Cook stoves; CFD; Pyrolysis; Biomass; 1 d heat conduction

1. Introduction

Experimental investigations on a pulverised fuel stove with high efficiency and low emissions were reported in part I [1]. This stove functioned in gasification mode for about 30 min, a mode in which clean combustion was observed at the port exit. During this period no flame was observed within the port of the stove. Beyond this duration, the flame flashed back into the port and the flame at port exit was observed to be mildly sooty. To understand this behaviour, computational investigations were conducted in the condensed phase (fuel block region) and gas phase (port region) of the stove. This paper reports the results of computational investigations and comparisons with experimental results.

*Corresponding author.
E-mail address: dixit@cgpl.iisc.ernet.in (C.S.B. Dixit).

0961-9534/$ - see front matter © 2006 Elsevier Ltd. All rights reserved.
doi:10.1016/j.biombioe.2006.01.010

2. C-phase analysis

A formulation of the problem of one dimensional pyrolysis front propagation is given in [2]. Considering the fact that heat transfer is the controlling feature in the propagation of pyrolysis front a frame work is chosen here to obtain the propagation rates based on energy balance at the pyrolysis front for unsteady one-dimensional heat conduction.

Considering energy balance at the pyrolysis front shown in Fig. 1:

Enthalpy of pyrolysis products + product heat gain
= enthalpy of biomass + biomass heat gain.

Products of pyrolysis, volatiles and char, gain heat from char bed and wood gains heat from the front:

$$\rho_p \dot{r}[fh_v + (1-f)h_c] + k_c T_{,r}\big|_c = \rho_p \dot{r} h_w + k_w T_{,r}\big|_w,$$

Nomenclature

$\bar{k}$	average conductivity of porous bed, $W m^{-1} K^{-1}$	c_{pw}	specific heat of green biomass
ΔH	heat of reaction for pyrolysis of wood, $J kg^{-1}$	f	fraction volatilised
$\dot{m}$	mass loss rate per unit height of the bed, $kg m^{-1} s^{-1}$	g	acceleration due to gravity $m s^{-2}$
$\dot{r}$	pyrolysis front propagation rate, $m s^{-1}$	h	heat transfer coefficient, $W m^{-2} K^{-1}$
ε	porosity, see Eq. (16)	h_c	enthalpy of char, $J kg^{-1}$
μ	dynamic viscosity, Pa s	h_v	enthalpy of volatiles, $J kg^{-1}$
v	kinematic viscosity, $m^2 s^{-1}$	h_w	enthalpy of wood, $J kg^{-1}$
ρ_p	loading density of the pulverised fuel, $kg m^{-3}$	k_c	conductivity of hot char, $W m^{-1} K^{-1}$
Gr	Grashof number	k_w	conductivity of wood, $W m^{-1} K^{-1}$
Pr	Prandtl number	r	radius, mm
B	blocking effect, see Eq. (18)	r^*	radius of the pyrolysis front, m
c_p	specific heat of pyrolysis gases, $J kg^{-1} K^{-1}$	T^*	temperature of the pyrolysis front, K
		T_g	gas temperature, K
		T_s	port surface temperature, K
		Nu	Nusselt number
		$,r$	d/dr

where $\rho_p$is the loading density of the pulverised fuel, $kg m^{-3}$, $\dot{r}$ the pyrolysis front propagation rate, $m s^{-1}$, f the fraction volatilised, h_v the enthalpy of volatiles, $J kg^{-1}$, h_c the enthalpy of char, $J kg^{-1}$, h_w the enthalpy of wood, $J kg^{-1}$, k_c the conductivity of hot char, $W m^{-1} K^{-1}$, and k_w the conductivity of wood, $W m^{-1} K^{-1}$. Subscript c denotes char and subscript w is used for wood. This is simplified to $\rho_p \dot{r}[f h_v + (1-f)h_c - h_w] = k_w T_{,r}|_w - k_c T_{,r}|_c$. Therefore,

$$\rho_p \dot{r} \Delta H = k_w T_{,r}\big|_{w,r=r^*} - k_c T_{,r}\big|_{c,r=r^*}, \tag{1}$$

where ΔH is the heat of reaction of pyrolysis of wood $J kg^{-1}$ and superscript * is used to denote position and properties of pyrolysis front.

The temperature gradients are evaluated as follows. Consider the char zone. The following assumptions are made:

1. Temperature of char and pyrolysis gases are same.
2. Processes are quasi-steady.
3. Thermal conductivity is constant.

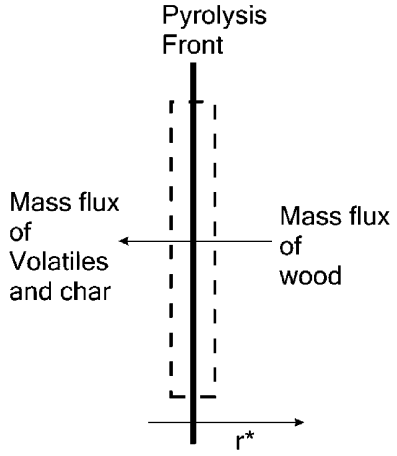

Fig. 1. Mass balance at the pyrolysis front.

4. Pyrolysis front movement is neglected compared to the velocity of pyrolysis gases.

The products of pyrolysis generated in the pyrolysis zone move through the porous char zone radially inwards, absorbing heat from char zone to get released into the port at T_s. Neglecting the temperature dependence of conductivity the quasi-steady conduction equation for char zone becomes

$$(rT_{,r})_{,r}/r + \dot{m} c_p T_{,r}/(2\pi r k_c) = 0, \tag{2}$$

where $\dot{m}$ is the mass loss rate per unit height of the bed $kg m^{-1} s^{-1}$ and c_p the specific heat, $J kg^{-1} K^{-1}$ of pyrolysis gases. The boundary conditions are at $r = a$,

$$h(T_g - T_s) = -k_c T_{,r}, \tag{3}$$

where h is the free convection heat transfer coefficient, $W m^{-2} K^{-1}$, T_g the gas temperature, K, within the port and T_s the port surface temperature. At $r = r^*$, $T = T^*$. Temperature distribution in char zone is obtained as

$$T = C_2 - \frac{C_1}{r^c}, \tag{4}$$

where

$$c = \frac{\dot{m} c_p}{2\pi k_c} = \frac{2\pi r^* \rho_p \dot{r} c_p f}{2\pi k_c} = \frac{f \rho_p c_p}{k_c} \dot{r} r^* = D \dot{r} r^*, \tag{5}$$

where f is the fraction of volatiles leaving the fuel bed:

$$C_1 = \frac{T^* - T_g}{\frac{1}{a^c} + \frac{k_c}{h a^{1+c}} - \frac{1}{r^{*c}}}, \tag{6}$$

$$C_2 = T^* + \frac{C_1}{r^{*c}} \tag{7}$$

and temperature gradient in char zone is obtained as

$$T_{,r} = \frac{C_1}{r^{1+c}}. \tag{8}$$

Similarly, the unpyrolysed fuel region receives heat from pyrolysis front at location r^* and temperature T^* moving radially outwards. Let the radial coordinate for biomass region be r' so that $r' = r - r^*$. Therefore, conduction equation for this region is written as

$$[(r' + r^*)T_{,r'}]_{,r'}/(r' + r^*) + \rho c_{\mathrm{pw}} \dot{r} T_{,r'}/k_{\mathrm{w}} = 0, \tag{9}$$

where c_{pw} is the specific heat of green biomass. The boundary conditions are at $r' = 0$, $T = T^*$ and at $r' = \infty$, $T = T_\infty$. The temperature distribution is given by

$$\frac{T - T^*}{T_\infty - T^*} = \frac{\int_0^{r'} \frac{\exp(-c_{\mathrm{w}} z)}{r^* + z}\,\mathrm{d}z}{\int_0^{\infty} \frac{\exp(-c_{\mathrm{w}} z)}{r^* + z}\,\mathrm{d}z}. \tag{10}$$

The temperature gradient is given by

$$T_{,r'} = \frac{(T_\infty - T^*)\exp(-c_{\mathrm{w}} r')}{(r^* + r')\int_0^{\infty} \frac{\exp(-c_{\mathrm{w}} z)}{r^* + z}\,\mathrm{d}z}. \tag{11}$$

The integral in the denominator is re-written in terms of exponential integral, $E_1()$ as

$$\int_0^{\infty} \frac{\exp(-c_w z)}{r^* + z}\,\mathrm{d}z = \exp(c_{\mathrm{w}} r^*) \int_1^{\infty} \frac{\exp(-c_{\mathrm{w}} r^* y)}{y}\,\mathrm{d}y = \exp(c_{\mathrm{w}} r^*) E_1(c_{\mathrm{w}} r^*), \tag{12}$$

where

$$c_{\mathrm{w}} = \frac{\rho_{\mathrm{p}} c_{\mathrm{pw}}}{k_{\mathrm{w}}} \dot{r} = D_{\mathrm{w}} \dot{r}. \tag{13}$$

Substituting (8) and (11) in (1) we have

$$\rho_{\mathrm{p}} \dot{r} \Delta H = \frac{k_{\mathrm{w}}(T_\infty - T^*)}{r^* \exp(c_{\mathrm{w}} r^*) E_1(c_{\mathrm{w}} r^*)} - \frac{k_{\mathrm{c}} C_1}{r^{*1+c}}. \tag{14}$$

Time taken for the front to travel between any two radial positions r_1* and r_2* is obtained as

$$t = \rho_{\mathrm{p}}(\Delta H) \int_{r_1^*}^{r_2^*} \frac{r^*\,\mathrm{d}r^*}{\frac{k_{\mathrm{w}}(T_\infty - T^*)}{\exp(D_{\mathrm{w}} \dot{r} r^*) E_1(D_{\mathrm{w}} \dot{r} r^*)}} - \frac{k_{\mathrm{c}}(T^* - T_{\mathrm{g}})}{\left(1 + \frac{k_{\mathrm{c}}}{ha}\right)\left(\frac{r^*}{a}\right)^{D \dot{r} r^*} - 1} \tag{15}$$

with $\dot{r}$ obtained from (14) for each value of r*. The approximation for the function $E_1(x)$ where x is $c_{\mathrm{w}} r^*$ is obtained from [3].

The packing density of biomass was $\rho_{\mathrm{p}} = 250\,\mathrm{kg\,m^{-3}}$. The reported heat of reaction ΔH for wood pyrolysis is in the range -160 to $200\,\mathrm{J\,g^{-1}}$ [4,5]. A measurement of heat of reaction of the sample used for experiment was tested for heat of reaction using digital scanning calorimetry (DSC). The data indicates pyrolysis to be exothermic with a heat of reaction of about $-120\,\mathrm{J\,g^{-1}}$. The values of various physical constants used are as follows: $c_{\mathrm{p(char)}} = 1250\,\mathrm{J\,kg^{-1}\,K^{-1}}$, $k_{\mathrm{char}} = 0.4\,\mathrm{W\,m^{-1}\,K^{-1}}$, $k_{\mathrm{gas,800\,K}} = 0.04\,\mathrm{W\,m^{-1}\,K^{-1}}$, $\varepsilon_{\mathrm{char}} = 0.9$, $c_{\mathrm{pwood}} = 2400\,\mathrm{J\,kg^{-1}\,K^{-1}}$, $k_{\mathrm{biomass}} = 0.168\,\mathrm{W\,m^{-1}\,K^{-1}}$, $k_{\mathrm{air,300\,K}} = 0.02\,\mathrm{W\,m^{-1}\,K^{-1}}$, $\varepsilon_{\mathrm{wood}} = 0.6$. Porosity of pulverised fuel bed was approximated based on particle density of biomass used ($\sim$600 kg m^{-3}) and packing density of fuel bed during experiment. Porosity of char bed was estimated based on intrinsic char density of 1600 kg m^{-3}, assuming 20% of initial biomass is left behind as char. Most of parameters have been chosen from available sources [4,6,7]. The average conductivity of porous bed is obtained from [4] as

$$\bar{k} = k_{\mathrm{c}}(1 - \varepsilon) + \varepsilon k, \tag{16}$$

where k_{c} is the conductivity of solid, k the conductivity of gas in the pores and ε the porosity, the fraction of gas volume in total volume.

The free convection heat transfer coefficient was estimated from correlation for vertical plates:

$$Nu = 0.59(Gr\,Pr)^{0.25}, \tag{17}$$

where Nusselt number $Nu = hx/k$, x is the vertical distance, Grashoff number $Gr = gx^3(T_{\mathrm{f}} - T_0)/(T_0 v^2)$, and Prandtl number $Pr = \mu c_{\mathrm{p}}/k$ with fluid properties evaluated at mean fluid temperature. The convective heat flux to the port wall from g-phase is subjected to a blocking effect by the mass flux from the port wall (mass flux causes the boundary layer to thicken resulting in reduced gradients) This results in a reduction of heat transfer coefficient. This reduction in heat transfer coefficient is taken into account in the following manner. The required heat transfer coefficient, h is

$$\frac{h}{h_0} = \frac{\ln(1 + B)}{B}, \tag{18}$$

where $B = \rho v c_{\mathrm{p}}/h$ [8]. Let $B_0 = \rho v c_{\mathrm{p}}/h_0$ where ρv is the volatile mass flux $f \rho_{\mathrm{p}} \dot{r}$. Eq. (18) is rewritten in terms of B_0 as

$$\frac{h}{h_0} = \frac{B_0}{\exp\, B_0 - 1} \tag{19}$$

from which heat transfer coefficient h at any given $\dot{r}$ can be obtained.

The radius of pyrolysis front r* as a function of time t, obtained from Eq. (15), is plotted in Fig. 2 as the solid lines for the range of heats of reaction for wood pyrolysis reported in literature. The experimentally obtained position of r* as a function of time from [1] is also shown. The experimental results are in agreement with theory. The burn rates with measured values of heat of pyrolysis of $-120\,\mathrm{kJ\,kg^{-1}}$ provides best fit to the experimentally determined burn rates.

The radial temperature distribution in char region ($r/r^* < 1$) and in biomass region($r/r^* > 1$) obtained from Eqs. (4) and (10) are plotted in Fig. 3(a)–(e) with radial positions normalised by the radius of the pyrolysis front r*. The experimental data plotted are for times corresponding to radius of pyrolysis front r* indicated in Fig. 7(c) of [1]. Theoretical predictions seem to be in broad agreement with the experimental data.

C-phase temperatures as a function of time obtained from Eq. (15) at a location 2 mm into c-phase is plotted in Fig. 4. Theoretical plot starts from the time when the location 2 mm inside c-phase reaches 580 K. Experimental data from c-phase temperature history 2 mm inside c-phase reported in [1] is also plotted for comparison. Predicted

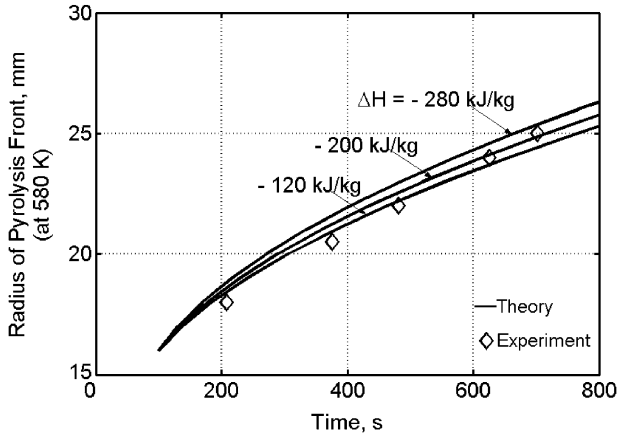

Fig. 2. Radius of pyrolysis front as a function of time. Computed values are shown for three heats of reaction.

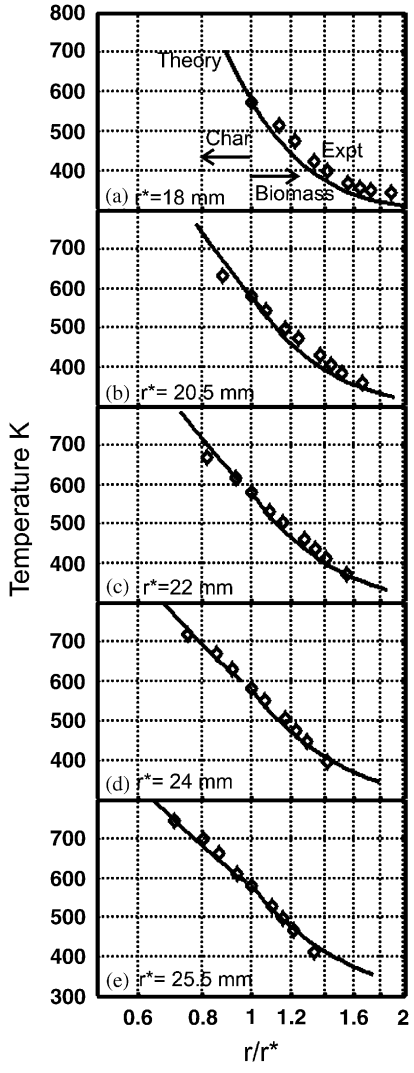

Fig. 3. (a–e) Radial temperature distribution at several positions of pyrolysis front.

values correspond to c-phase temperatures for pyrolysis front positions at higher times because in theoretical calculations, pyrolysis front movement is neglected compared to pyrolysis gas movement rate. This causes predicted values to be higher then measured values. Measured surface temperature values could be lower than the predicted values also due to conduction loss from the measuring junction through thermocouple wires.

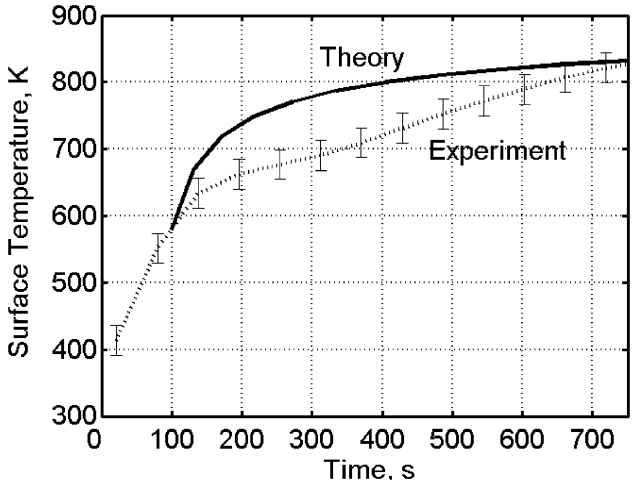

Fig. 4. C-phase temperature as a function of time at a location 65 mm below the port exit and 2 mm into c-phase.

3. Computational modelling of G-phase

A port of a tube stove with 40 mm diameter and AR of 6 was chosen for modelling aimed at understanding the distinction between gasification and combustion modes. A commercial CFD code *CFX-TASCflow* was used for this study. The region selected included the fuel port, the tangential air inlet, secondary air inlet and the combustion device of a single port tangential inlet stove. To ensure proper simulation of exit conditions certain extra region over the port exit was also included in the computation. The 3-D reactive flow with natural convection in this domain was modelled. Figs. 5(a) and (b) show the schematic of the computational domain used for combustion mode and gasification mode simulations, respectively.

The boundary conditions used for the computation are also shown in the figures. It was assumed that the g-phase was subjected to steady boundary conditions for the purpose of computation in both the simulations.

The two air inlets—primary (bottom) and secondary (shown in Figs. 5(a) and (b)) were treated as constant total pressure inlets. Gasification air inlet was 6 mm wide × 30 mm high and was provided such that air enters the port in a tangential direction similar to inlet structure used during experimentation. The secondary air inlet was essentially the gap between the combustion device and the top surface of the fuel block which was about 10 mm. The circumferential region 10 mm high above the fuel port wall was treated as secondary air inlet.

The boundary of entire region simulated above the fuel port was treated as an opening subjected to mixed flow

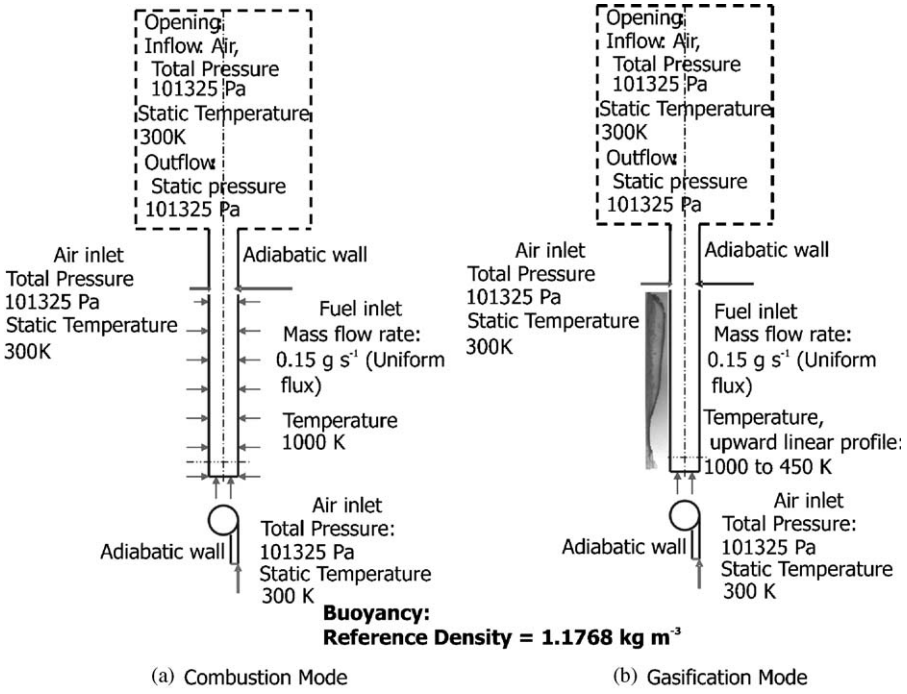

Fig. 5. The computational domain along with boundary conditions and initial conditions used during combustion and gasification mode computations are shown in (a) and (b).

boundary condition. That is, for in-flow the fluid was assumed to be air at a total pressure of 101,325 Pa and static temperature 300 K while the products went out at a static pressure of 101,325 Pa.

The circumferential region above secondary air inlet up to fuel port exit was treated as adiabatic wall (see Figs. 5(a) and (b)).

The entire fuel port wall was treated as fuel inlet with fuel flux directed radially inwards. The experimentally observed typical mass loss rate for the port configuration chosen (40 mm diameter, AR = 6) was $\sim 0.15\,g\,s^{-1}$. The mass loss rate during gasification mode operation was about 10–15% lower. For the purpose of simulation it was assumed during both combustion and gasification mode operations the fuel mass flow rate was constant at $0.15\,g\,s^{-1}$.

The mass flow distribution in the vertical direction was not uniform during gasification mode operation. It was experimentally determined that the mass flux from bottom region of the stove was larger. This can be seen by the photograph of the profile of the pyrolysis front at the end of 30 min of stove operation shown in Fig. 5(b). From this profile it was possible to estimate the fuel flux as a function of vertical distance. Total mass loss rate during this period was determined experimentally as $0.15\,g\,s^{-1}$ remaining uniform for the complete duration of 30 min. Mass loss at any given vertical position is directly proportional to the depth of penetration of the pyrolysis front into the fuel block. The depth of penetration was measured from the char profile at discrete vertical intervals of 5 mm. The total mass loss rate was distributed in the same proportion as the depth of penetration. From this, fuel flow rate from each 5 mm section is known. Using this fuel flow rate, fuel flux from the port wall was determined. This was incorporated into the boundary condition during gasification mode operation with fuel inflow given as a profile matching with the experimentally observed mass flux. Fig. 6 shows the experimentally determined fuel flux profile.

For combustion mode operation, the onset of which took place after 30 min of stove operation it was observed that fuel flux distribution in the vertical direction was more uniform since the entire port surface was active. The flux distribution determined from pyrolysis front data shown in Fig. 5(b) of [1] is presented in Fig. 6. The flux distribution is found to be nearly uniform. Therefore, uniform vertical fuel flux of $0.0045\,kg\,m^{-2}\,s^{-1}$ which corresponds to a fuel mass flow rate of $0.15\,g\,s^{-1}$ from the port wall was employed.

It was observed that port surface temperature distribution in the vertical region was such that temperatures in the bottom region was higher during the beginning of stove operation. Port surface temperatures were assumed to vary linearly from 450 to 1000 K during gasification mode functioning. During the experiment measuring junction of thermocouple was placed flush with the port surface. It was observed that during stove operation, port surface receded uncovering the measuring junction to g-phase. Thus, information on surface temperatures during combustion mode was not available. For simplicity, it was assumed that the port surface was at a uniform value of 1000 K during combustion mode operation.

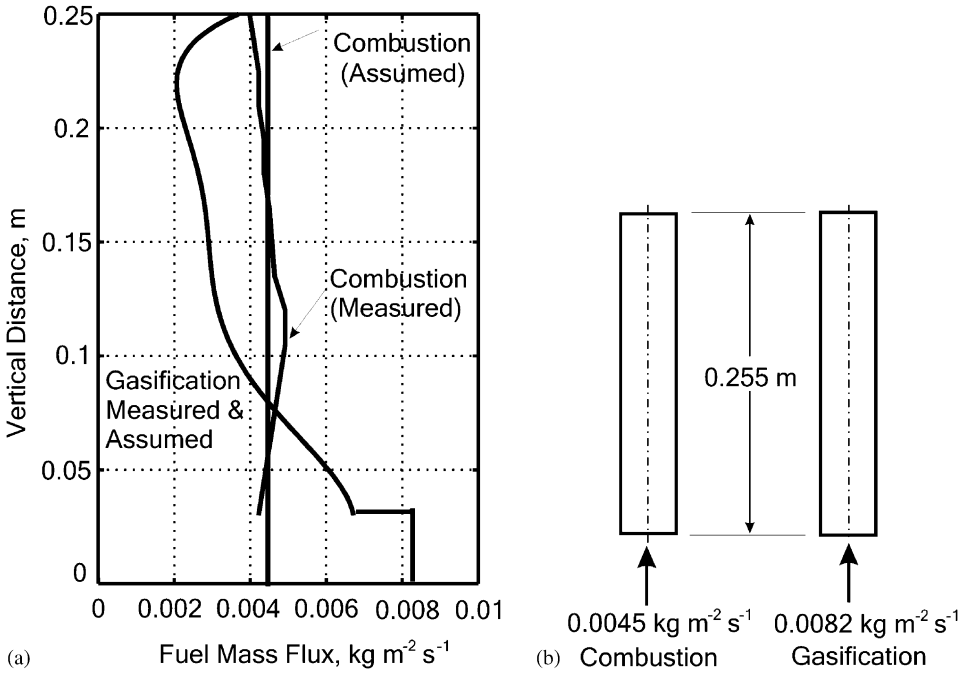

Fig. 6. (a) The fuel mass flux distribution during simulation of combustion and gasification modes of operation. (b) Shows the fuel flux from the bottom plane.

The composition of biomass is $CH_{1.4}O_{0.58}N_{0.001}$ [8] on ash free basis. For computational purposes nitrogen content was ignored. During the stove operation volatiles generated during pyrolysis entered the port. Volatiles constitute about 80% of total ash-free fuel mass with 20% carbon left behind. Thus, 1 mol of volatiles generated from the biomass with molecular composition defined above would contain ~7.46 g (0.62 mol) carbon ~1.4 g (1.4 mol) hydrogen and ~9.28 g (0.58 mol) oxygen. From this, volatile molecule could be estimated to contain $CH_{2.2}O_{0.93}$. For computation, the approximate composition of fuel was chosen as CH_2O.

The energy content of volatiles was estimated based on total energy content of biomass and energy content of carbon that was left behind [9]. Heat of formation of volatiles is found as $h_{f,CH_2O} = -276\,\mathrm{MJ\,kmol^{-1}}$. The ambient density was taken as $1.18\,\mathrm{kg\,m^{-3}}$. The fuel flow, total flow and air-to-fuel ratios integrated over the area normal to flow direction (z direction) during gasification mode operation is presented in Fig. 7.

The increase in total flow from 0 to 30 mm is due to air entry from gasification air inlet. The air-to-fuel ratio becomes stoichiometric ($a/f = 6.3$) at 25 mm height and drops continuously as the oxygen in flow stream is fully depleted by 100 mm height during gasification mode operation. Gasification air flow was $0.16\,\mathrm{g\,s^{-1}}$. This corresponds to 17% of stoichiometric air requirement on overall basis. Secondary air flow was $0.15\,\mathrm{g\,s^{-1}}$. This implies that complete combustion will need air from the atmosphere and the flame will stand much above the combustion device similar to the experiments.

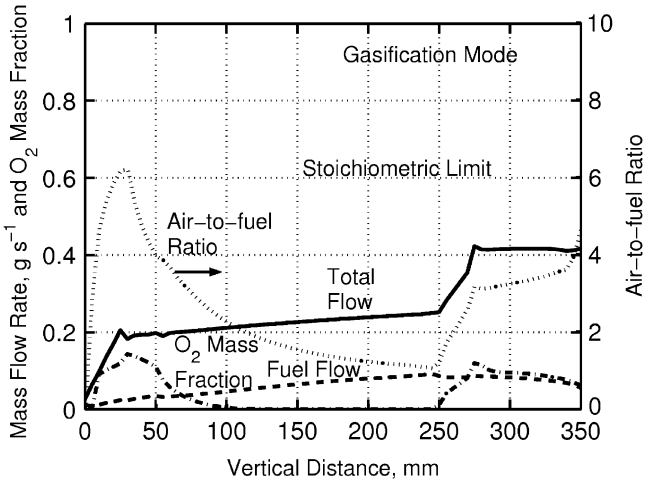

Fig. 7. Total mass flow rate, fuel flow rate, air-to-fuel ratio and oxygen mass fraction averaged over flow cross section plotted during gasification mode operation.

Fig. 8 shows the flow parameters total flow, fuel flow and air-to-fuel ratio as a function of vertical distance during combustion mode operation. The air-to-fuel ratio, integrated over port cross section during combustion mode operation, was very lean ($a/f = 48$) in the inlet region. Air-to-fuel ratio became stoichiometric at 100 mm height and combustion continued in the port region.

The air inflow from gasification air inlet was $0.19\,\mathrm{g\,s^{-1}}$. This is 20% of stoichiometric air requirement of the fuel supplied. The air inflow during gasification mode operation was about 15% lower than combustion mode operation.

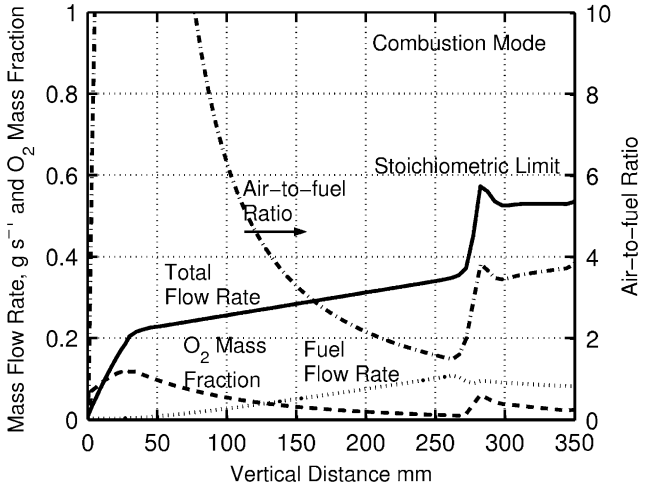

Fig. 8. Total mass flow rate, fuel flow rate, air-to-fuel ratio and oxygen mass fraction averaged over flow cross section plotted during combustion mode operation.

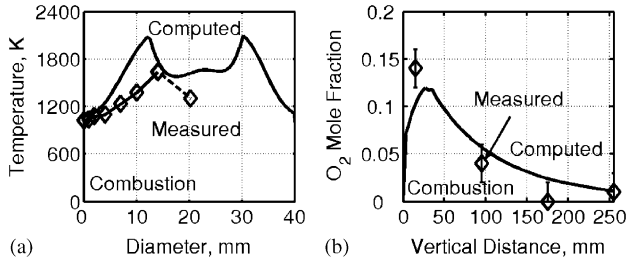

Fig. 9. Comparison of computed and experimental temperature and oxygen fraction during combustion mode operation. (a) Shows comparison of g-phase temperatures along the radius of the fuel port at a location 40 mm below port exit. (b) Shows comparison of g-phase oxygen fraction along the axis of fuel port.

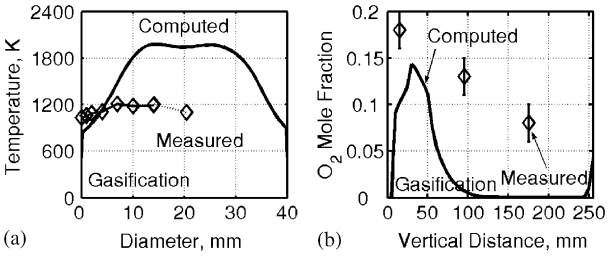

Fig. 10. Comparison of computed and experimental temperature and oxygen fraction during gasification mode operation. (a) Shows comparison of g-phase temperatures along the radius of the fuel port at a location 40 mm below port exit. (b) Shows comparison of g-phase oxygen fraction along the axis of fuel port.

This may be because the fuel flux through the bottom region is relatively higher in gasification mode operation and part of the driving force due to buoyancy is utilised in transporting fuel from bottom region to the port exit resulting in reduction of air ingestion. Once the fuel flow in combustion mode becomes more uniformly distributed, air inflow from bottom inlet increases since the available suction which was being utilised to lift fuel from bottom region is shifted to air inlet. Secondary air flow is nearly same in both the cases.

The rate parameters used for predicting the reaction rate, activation energy and pre-exponential factors depend upon the equivalence ratio [10]. The present simulation was carried out with a constant reaction rate corresponding to stoichiometry. This has resulted in higher predicted g-phase temperatures in this region than that expected.

The comparison of predicted and measured temperature and oxygen concentrations during combustion mode operation is presented in Fig. 9(a) and (b).

The predicted temperatures are in qualitative agreement with the measured values though the peak temperature is higher by 350 K. One clear reason is that during computation single step forward reaction without dissociation was considered. With dissociation the predicted temperatures will be lower. The measured oxygen concentration as shown in Fig. 9(b) is in agreement with predicted values which implies that lower measured temperatures must be due to dissociation only.

The comparison of predicted and measured temperature and oxygen concentrations during gasification mode operation is presented in Fig. 10(a) and (b).

In this case, there are significant differences between predictions and measurements. It was observed that centre line temperature increases and oxygen fraction decreases when the flame flash back occurs. However, the predictions show the opposite trend. It is clear from the experimental data that during gasification mode operation the g-phase reactions are nearly absent. There is no significant difference in surface temperature between gasification and combustion. The possible explanation for this behaviour is that the species such as hydrogen and to some extent carbon monoxide react while the large molecular mass pyrolysis products remain unreacted. The reactions between species such as hydrogen and oxygen have relatively low activation energy compared to those between large molecular mass pyrolysis gases and oxygen. Therefore, hydrogen and to certain extent carbon monoxide are oxidised while the high molecular mass compounds remain unreacted unless high temperature zone is present. These factors are not predicted in the numerical computations because of the use of single step forward chemistry model.

These observations are strengthened by the fact that in many cases the gasification mode is induced closing the inlet port and forcing the flame to quench in the port though there are cases where spontaneous transition from combustion to gasification mode has taken place.

Further as can be seen from Figs. 9(a) and 10(a) the temperature gradient normal to the surface is significantly lower in the case of gasification mode compared to combustion. Yet, the fuel consumption rate and the surface temperature are significantly different between the two cases in spite of the large change in heat flux to the surface. The possible explanation for this behaviour can be given

from the fact that the oxygen concentration at the surface is large in the gasification mode while oxygen will be consumed in the flame in the case of combustion mode. Hence, in gasification mode fuel consumption rate is sustained by the reaction between oxygen and char, while in combustion mode the fuel consumption is sustained by heat flux from the flame.

Two steady-state calculations were made to simulate combustion and gasification modes of stove operations with several simplifying assumptions. The computational study confirms that gasification phenomena was due to larger fuel release that take place from the bottom region during the early part of stove operation.

As the stove operation continues in gasification mode, port surface temperatures become uniform with upper regions becoming active. Fuel flux from the bottom region is reduced, possibly due to exhaustion of volatile content. Under these conditions the stove will draw more air since available buoyancy force would get used to lift more air from gasification air inlet at the bottom causing combustion mode operation.

4. Summary

An analysis carried out on the c-phase thermal profile with moving pyrolysis front showed that the predicted temperature profiles and the pyrolysis front movement rates compared excellently with the measured data.

3D modelling of the g-phase of tangential inlet single port tube stove was done using CFD calculations. The computational study confirms that gasification phenomena was due to larger fuel release that took place from the bottom region during the early part of stove operation.

References

[1] Dixit CSB, Paul PJ, Mukunda HS. Part I: Experimental studies on a pulverized fuel stove. Biomass and Bioenergy, in press, doi:10.1016/j.biombioe.2006.01.011.
[2] Ohlemiller TJ. Modeling of smouldering combustion propagation. Progress in Energy and Combustion Science 1985;11(4):277–310.
[3] Abramowitz M, Stegun I. Hand book of mathematical functions. Applied Mathematics Series, National Bureau of Standards, 1964.
[4] Mukunda HS, Paul PJ, Srinivasa U, Rajan NKS. Combustion of wooden spheres—experiments and model analysis. Twentieth Symposium (International) on Combustion 1984:1619–28.
[5] Kanury AM, Blackshear PL. On the combustion of wood 2: the influence of internal convection on the transient pyrolysis of cellulose. Combustion Science and Technology 1970;2:5–9.
[6] Holman JP. Heat transfer. McGraw-Hill Book Company. 2nd ed. 1989.
[7] Perry RH, Chilton CH. Chemical engineer's hand book, 5th ed. Kogakusha: McGraw-Hill; 1973.
[8] Mukunda HS. Understanding combustion. IIT Madras series in science and engineering. New York: Macmillan; 1989.
[9] Dixit CSB. Experimental and computational studies on a pulverized fuel stove. PhD thesis, Indian Institute of Science, August 2003.
[10] Coffee TP, Kotlar AJ, Miller MS. The overall reaction concept in premixed, laminar, steady-state flames 1: stoichiometries. Combustion and Flame 1983;54:155–69.